Evolution of the Interplanetary Turbulence and the Associated Turbulence Anisotropy in the Outer Heliosphere: VOYAGER 2 Observations

Xingyu Zhu[2] , Jiansen He[1] , Gary P. Zank[2,3] , Daniel Verscharen[4] , Ling-Ling Zhao[2,3] , Die Duan[1] , and Rong Lin[1]

[1] School of Earth and Space Sciences, Peking University, Beijing 100871, People's Republic of China; jshept@pku.edu.cn
[2] Center for Space Plasma and Aeronomic Research (CSPAR), The University of Alabama in Huntsville, Huntsville, AL 35805, USA
[3] Department of Space Science, The University of Alabama in Huntsville, Huntsville, AL 35805, USA
[4] Mullard Space Science Laboratory, University College London, Dorking RH5 6NT, UK

Abstract

We study the radial evolution of the inertial-range solar wind plasma turbulence and its anisotropy in the outer heliosphere. We use magnetic field ($\boldsymbol{B}$) measurements from the Voyager 2 spacecraft for heliocentric distances R from 1 to 33 au. We find that the perpendicular and trace power spectral densities (PSDs) of the magnetic field ($E_{B_\perp}$ and $E_{B_{Tr}}$) still follow a Kolmogorov-like spectrum until 33 au. The parallel magnetic field PSD, $E_{B_\parallel}$, transits from a power-law index of -2 to $-5/3$ as the distance crosses $R \sim 10$ au. The PSD at frequencies 0.01 Hz $< f < 0.2$ Hz flattens at $R > 20$ au, gradually approaching an f^{-1} spectrum, probably due to instrument noise. At 0.002 Hz $< f < 0.1$ Hz, quasi-parallel propagation dominates at 1 au $< R < 7$ au, with quasi-perpendicular propagation gradually emerging at $R > 5$ au. For $R > 7$ au, oblique propagation becomes the primary mode of propagation. At smaller frequencies of $f < 0.01$ Hz, $E_{B_\perp}$ increases with propagation angle at 1 au $< R < 5$ au, and in contrast decreases with propagation angle at $R > 5$ au due to the enhanced power level at propagation angles smaller than $20°$. Such enhancement may derive from the injection of wave energy from the pickup ion source into the background turbulent cascade, and the injected wave energy is transferred across scales without leaving local enhancements in $E_{B_\perp}$ or $E_{B_{Tr}}$.

Unified Astronomy Thesaurus concepts: Heliosphere (711); Interplanetary turbulence (830); Solar wind (1534)

1. Introduction

The solar wind plasma is an intrinsically turbulent magnetohydrodynamic (MHD) medium (Coleman 1968; Tu & Marsch 1995; Bruno & Carbone 2013; Verscharen et al. 2019). The range of physical quantities is wide and spectra exhibit segmented power-law characteristics. A turbulent cascade leads to an inertial-range power-law spectrum between an energy-containing range at large scales and a steeper dissipation range at smaller scales (Kiyani et al. 2015). MHD turbulence actively and continuously evolves during the outward propagation of the solar wind (Zank et al. 1996), and magnetic field fluctuations show different evolutionary characteristics over different frequency ranges. From 0.3 to 1 au, the spectral power decays as $R^{-4.2}$ for $f > 2.5 \times 10^{-3}$ Hz but as $R^{-3.2}$ in the lower frequency range $f < 2.5 \times 10^{-3}$ Hz (Bavassano et al. 1982). Observations from the Parker Solar Probe (PSP) have shown that the magnetic field spectral index evolves from $-3/2$ at $R \sim 0.17$ au to $-5/3$ at $R \sim 1$ au (Chen et al. 2020). However, the spectral index is roughly stable and close to $-5/3$ beyond 1 au (Pine et al. 2020a). These results indicate that local physical processes potentially affect turbulent energy transport. The resultant radial evolution of power spectra exhibits period dependence.

Theoretical efforts have been made to account for the radial evolution of MHD fluctuations/turbulence. Wentzel–Kramers–Brillouin (WKB) theory (Whang 1973; Hollweg 1974) largely reproduces the radial decrease of fluctuation energy at large scales within approximately 10 au (Tu et al. 1984; Pine et al. 2020b;

Wu et al. 2021), but diverges quite significantly thereafter. This model assumes that the multiscale fluctuations are a superposition of noninteracting outward-propagating Alfvén waves, which leads to $\langle \delta B^2 \rangle \sim R^{-3}$, where $\langle \delta B^2 \rangle$ quantifies the magnetic field fluctuation energy density. However, WKB theory cannot explain the systematic changes in other quantities, such as the decrease in cross-helicity (Roberts et al. 1987; Iovieno et al. 2016; Parashar et al. 2020) with R. In order to model the radial evolution of MHD fluctuations self-consistently, a model must consider additional physical mechanisms, for instance, turbulence effects incorporating local nonlinear interactions and coupling to large-scale gradients (Zhou & Matthaeus 1989; Zank et al. 1996), or turbulence driven by partially reflected Alfvén waves (Heinemann & Olbert 1980; Velli 1993; Cranmer 2010; Chandran et al. 2011; Perez & Chandran 2013; van der Holst et al. 2014). In the outer heliosphere beyond the ionization cavity (Zank 1999, 2016; Sokół et al. 2019), interstellar pickup ions (PUIs) become a major driving source of Alfvénic fluctuations (Lee & Ip 1987; Williams & Zank 1994; Zank et al. 1996; Zank 1999; Zank et al. 2018; Sokół et al. 2022; Zirnstein et al. 2022). The PUI component is not absorbed by the background thermal solar wind plasma but provides a sufficient free energy source to excite unstable waves (e.g., sunward-propagating fast-mode waves; Zank 1999; Joyce et al. 2010; Smith et al. 2017; Hollick et al. 2018). Turbulence transport models (Zank et al. 1996; Isenberg et al. 2003, 2010; Usmanov et al. 2016; Zank et al. 2017; Adhikari et al. 2021) incorporating the PUI source often assume that the wave energy quickly enters the turbulent cascade. These models predict a flatter decay of turbulent energy ($\langle \delta B^2 \rangle \sim R^{-2}$) beyond $R \sim 10$ au which is consistent with observations (Zank et al. 2018). However, theoretical models hitherto lack discussion on how the PUI-associated energy is transported in wavevector space and thus how it affects the turbulent cascade process.

In the solar wind, the presence of a nonzero background magnetic field $\boldsymbol{B_0}$ influences the nature of turbulence and therefore causes an anisotropy of turbulent fluctuations parallel and perpendicular to $\boldsymbol{B_0}$ (Montgomery & Turner 1981; Shebalin et al. 1983; Goldreich & Sridhar 1995; Horbury et al. 2008; Zhu et al. 2019; Zank et al. 2020; Duan et al. 2021). As compared to the global mean magnetic field, the local mean magnetic field more intensely affects the fluctuation anisotropy (Cho & Vishniac 2000). It leads to a scale-dependent anisotropy, which means that the turbulent eddies are more elongated along the local mean magnetic field direction as the scale becomes smaller (Podesta 2009). This scale dependence is consistent with the critically balanced scaling law $k_\parallel \sim k_\perp^{2/3}$ (Goldreich & Sridhar 1995, 1997), where $k_\parallel$ and $k_\perp$ are wavenumbers parallel and perpendicular to the local mean magnetic field, respectively. The principle of this theory is based on strong nonlinear interactions between balanced counterpropagating Alfvén wave packets. This zero cross-helicity scenario is broadly inconsistent with observations (Chen et al. 2013; Wicks et al. 2013; Telloni et al. 2019; Zhao et al. 2020). However, it still provides important insight into our understanding of solar wind turbulence.

Observations also reveal that solar wind MHD turbulence can be interpreted through a "slab + 2D" model (Matthaeus et al. 1990; Zank & Matthaeus 1992, 1993; Bieber et al. 1996; Dasso et al. 2005; Zank et al. 2017, 2020; Bandyopadhyay & McComas 2021). This model describes fluctuations as consisting of a parallel wave-like slab component ($k_\perp = 0$) and a perpendicular 2D turbulence component ($k_\parallel = 0$). For inertial-range turbulence, the ratio of 2D to slab energy is about 50/50 close to the Sun within 0.3 au (Bandyopadhyay & McComas 2021; Zhao et al. 2021) and evolves to about 80/20 at $R \sim 1$ au (Bieber et al. 1996; Adhikari et al. 2020). Zank et al. (2017) develop a model based on Zank & Matthaeus (1992, 1993), with a decomposition of fluctuations into slab and 2D components, describing the radial evolution of slab and 2D components in the heliosphere. This model, including stream-shear driving and a PUI source, predicts results consistent with observations from Voyager 2 (Zank et al. 2018). Based on this model, in the outer heliosphere, this ratio slightly increases until 8 au and then rapidly decreases until ~30 au (Adhikari et al. 2017). Although there are many studies of turbulence anisotropy in the inner heliosphere, the radial evolution of turbulence anisotropy in the outer heliosphere remains unclear. The PUI driving source can be an essential factor for the turbulent dynamics in the outer heliosphere. It is important to find observational evidence of how PUIs participate in the turbulent cascade and regulate turbulence anisotropy. This is required when wave signatures gradually vanish in the turbulent spectra, suggesting that the wave energy is "assimilated" by the background turbulence. Only in this case can we actually study the transport of energy associated with the PUI driving source based on observations.

In this work, we investigate the radial evolution of magnetic field power spectral densities (PSDs) at different scales in the inertial range. We also study the fluctuation anisotropy in terms of the distributions of propagation angle, average PSDs, and spectral index in different heliocentric distance ranges in the outer heliosphere. In Section 2, we introduce the methods used in the paper. Section 3 shows the radial evolution of the PSDs. Section 4 presents the fluctuation anisotropy at different heliocentric distance ranges. We summarize and discuss the observational results in Section 6.

2. Data and Analysis Method

2.1. Instrument and Data Selection

We use the magnetic field data with a cadence of 1.92 s (Behannon et al. 1977) measured by Voyager 2's Triaxial Fluxgate Magnetometer from 1977 August 24 to 1990 December 8. During this time interval, Voyager 2 cruised from 1 au to about 33 au. In heliographic inertial coordinates, the trajectory of Voyager 2 experiences a rapid variation in longitude within 10 au and slow change beyond 10 au (Figure 1(a)). The latitudinal position of the spacecraft is confined to within $\pm 10°$ around the solar ecliptic plane (Figure 1(b)).

The magnetic field data are irregularly distributed in time due to tracking gaps and interference from other instruments. They contain many data gaps, the occurrence and duration of which increase with R (Gallana et al. 2016). To avoid the influence of the data gaps on our results, we use the 305 intervals listed in Table 6 of Pine et al. (2020c). Most intervals last 3 hr and possess continuous magnetic field time series. This data set enables our calculation of wavelet spectra, the local mean magnetic field, and the propagation angle of the fluctuations without being affected by the data gaps.

Nonphysical spikes emerge intermittently in the time series of the magnetic field data. We implement a time-series Hampel filter (Pearson et al. 2016) to detect these nonphysical spikes with a window size of 60 points. We then remove points greater than 4 times the standard deviation, which we define as outliers. We only use this procedure to remove outliers rather than to replace them with median values. Removing the outliers leads to several short data gaps (~4 s) in the time series. The gap duration is less than 5% of the total time for each interval. In addition, we focus on fluctuations of less than 0.1 Hz in the spacecraft frame, which is greater than the individual short gap duration. Hence, the remaining small data gaps do not have a noticeable impact on our results. Figure 1(c) shows the time series of the magnetic field magnitude $|B|$ for all events after removal of the spikes. We convert time to heliocentric distance according to the position of Voyager 2.

2.2. Calculation of the Power Spectral Density and Local Mean Magnetic Field

After removing the spikes from the original magnetic field time series, we establish a new time series with equal time lag $t_n = t_0 + n\delta t$, where $\delta t = 1.92$ s and t_0 is the start time of the original time series for each interval. To study period-dependent fluctuations, we adopt a method based on wavelet decomposition (Torrence & Compo 1998) of the time series. This method has advantages when analyzing a time series with nonstationary power at multiple scales and has been widely used in studying solar wind turbulence (Horbury et al. 2008; He et al. 2012; Zhu et al. 2020). The discrete wavelet transform of the magnetic field component B_i at period τ_j and time t_n reads as

$$\tilde{B}_i(\tau_j, t_n) = \sum_{m=0}^{N-1} B_i(t_m)\psi^*\left(\frac{t_m - t_n}{\tau_j}\right), \qquad (1)$$
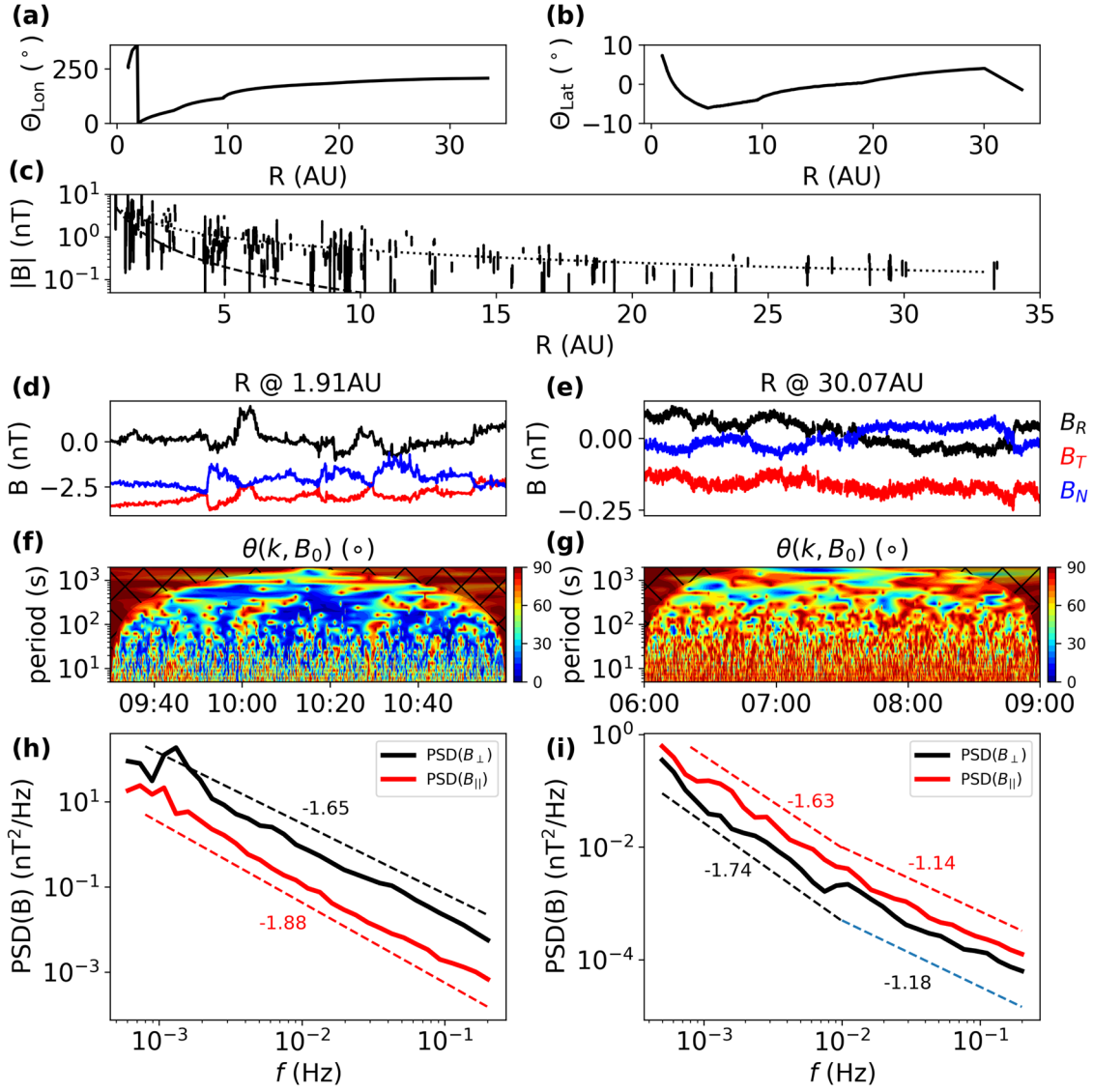
Figure 1. Position of Voyager 2, overview of the magnetic field magnitude $|B|$, and fluctuation properties at two distances. (a) Longitude of Voyager 2 as a function of heliocentric distance R in heliographic inertial coordinates. (b). Latitude of Voyager 2 as a function of heliocentric distance. (c) Measured magnetic field magnitude as a function of R for the 305 intervals studied. The dashed line represents R^{-2}, and the dotted line corresponds to R^{-1} for reference. (d)–(e) Time series of the R (black), T (red), and N (blue) magnetic field components for (d) case 1 and (e) case 2. (f)–(g) Time–period spectrogram of $\theta(\mathbf{k}, \mathbf{B}_0)$ for (f) case 1 and (g) case 2. The black shaded area denotes the cone of influence region. (h)–(i) Parallel (red) and perpendicular (black) time-averaged PSD for (h) case 1 and (i) case 2.

where j represents the jth period, n denotes the nth time step, and N is the total number of points. B_i can be each of the three orthogonal vector components in radial–tangential–normal (RTN) coordinates, B_R, B_T, and B_N, respectively. We calculate the wavelet coefficients at 32 periods, which are logarithmically spaced between 5 and 2000 s. ψ^* denotes the conjugate of the Morlet wavelet function

$$\psi(x) = \pi^{-\frac{1}{4}} e^{i\omega_0 x} e^{-\frac{x^2}{2}}, \qquad (2)$$

where $\omega_0 = 6$. For the Morlet wavelet functions, the period τ_j is related to the wavelet scale s_j by $\tau_j = 4\pi s_j / (\omega_0 + \sqrt{2 + \omega_0^2})$.

To obtain the different power levels in the parallel and perpendicular directions, we first calculate the local mean magnetic field. By weighting the time series with a Gaussian window profile centered at t_n, the local mean magnetic field at

t_n and τ_j is

$$\mathbf{B}_0(\tau_j, t_n) = \sum_{m=0}^{N-1} \mathbf{B}(t_m) \exp\left[-\frac{(t_n - t_m)^2}{2s_j^2}\right] \qquad (3)$$

(Podesta 2009). The parallel magnetic field wavelet coefficient $\tilde{B}_\parallel$ is the sum of the projection of the wavelet coefficient vectors onto the local mean magnetic field direction $\hat{\mathbf{e}}_{B_0} = \mathbf{B}_0 / |\mathbf{B}_0|$, i.e., $\tilde{B}_\parallel = \tilde{\mathbf{B}} \cdot \hat{\mathbf{e}}_{B_0}$.

We use the wavelet coefficients to calculate the PSD as

$$E_{B_i}(\tau_j, t_n) = \left| \tilde{B}_i(\tau_j, t_n) \right|^2 \cdot 2 \cdot \delta t, \qquad (4)$$

where $|\cdot|$ denotes the modulus of a complex number. The trace PSD is thereby $E_{B_{Tr}} = E_{B_R} + E_{B_T} + E_{B_N}$. The averaged perpendicular PSD is defined as $E_{B_\perp} = (E_{B_{Tr}} - E_{B_\parallel})/2$. For each interval, we also calculate the time-averaged PSD τ_j

(corresponding to the frequency of f_j), $E_{B_i}(\tau_j)$ $(E_{B_i}(f_j))$. Since the length of the time series is finite, the wavelet spectrum has a cone of influence region where edge effects become important. We exclude points in the cone of influence when calculating the time-averaged PSDs.

2.3. Calculation of the Angle between the Wavevector and Local Mean Magnetic Field

To calculate the wavevector ($\boldsymbol{k}$) direction $\hat{\boldsymbol{e}}_k$ relative to the local mean magnetic field, we employ the singular value decomposition (SVD) technique as described by Santolík et al. (2003). It solves a set of linearized equations based on the divergence-free condition for the magnetic field. It determines three singular value–singular vector pairs of a Hermitian spectral matrix of the magnetic field. The wavevector direction is determined by the direction of the vector associated with the minimum singular value. This allows us to estimate the angle between $\hat{\boldsymbol{e}}_k(\tau_j, t_n)$ and $\hat{\boldsymbol{e}}_{B_0}(\tau_j, t_n)$ as

$$\theta(\boldsymbol{k}, \boldsymbol{B}_0)(\tau_j, t_n) = \arccos(\hat{\boldsymbol{e}}_k \cdot \hat{\boldsymbol{e}}_{B_0}). \qquad (5)$$

This technique cannot determine the magnitude of the wavevector but only resolve the wavevector direction, with an 180° ambiguity. Hence, the angle obtained by this technique lies in the range of 0°–90°.

3. Radial Evolution of Inertial-range Turbulence in the Outer Heliosphere

First, it is worthwhile to compare directly the fluctuation properties at a further distance to those close to 1 au. By doing this, we get an intuitive sense of the evolution of solar wind turbulence in the outer heliosphere. Figures 1(d)–(i) present the basic fluctuation properties for two representative cases at $R \sim 2$ au (1978 January 1 09:30–11:00) and $R \sim 30$ au (1989 August 10 06:00–09:00), respectively. These properties include the magnetic field time series, the distribution of $\theta(\boldsymbol{k}, \boldsymbol{B}_0)$, $E_{B_\parallel}$, and $E_{B_\perp}$.

At these two distances, the magnetic field is dominated by the nonradial components (B_T or B_N; Figures 1(d) and (e)). The average magnetic field magnitudes are 3.71 and 0.17 nT. In the period range of $10\,\mathrm{s} < \tau < 10^3\,\mathrm{s}$, the wavevector is primarily aligned with the local mean magnetic field at $R \sim 2$ au (Figure 1(f)), while at $R \sim 30$ au, the wavevector is mostly quasi perpendicular to the local mean magnetic field (Figure 1(g)). The distribution of $\theta(\boldsymbol{k}, \boldsymbol{B}_0)$ suggests that the relative intensity of the parallel and perpendicular fluctuations are different at these two distances. At $R \sim 2$ au, the perpendicular fluctuations dominate. The spectral index for $E_{B_\perp}$ is -1.65, while the spectral index for $E_{B_\parallel}$ is -1.88 (Figure 1(h)). In contrast, the compressive (parallel) fluctuations have power levels that are comparable to those of the perpendicular fluctuations ($E_{B_\parallel} \gtrsim E_{B_\perp}$) at $R \sim 30$ au (Figure 1(i)). This distinction indicates that the compressibility of the solar wind magnetic turbulence continuously increases during its evolution in the outer heliosphere. In this context, we define $E_{B_\perp} = (E_{B_{Tr}} - E_{B_\parallel})/2$, based on our definition as the ratio of square of parallel and perpendicular magnetic field fluctuations $\delta B_\parallel^2 / \delta B_\perp^2 = E_{B_\parallel} / 2E_{B_\perp}$. Hence, $E_{B_\parallel} > E_{B_\perp}$ does not necessarily mean $\delta B_\parallel^2 > \delta B_\perp^2$.

Both $E_{B_\parallel}$ and $E_{B_\perp}$ at $R \sim 30$ au show a double power-law shape. At spacecraft-frame frequencies f between 5×10^{-4} Hz
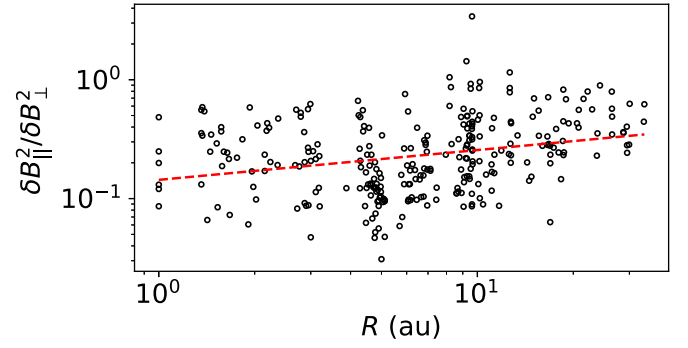

Figure 2. Ratio of the square of the parallel and perpendicular magnetic field fluctuations $\delta B_\parallel^2 / \delta B_\perp^2$ averaged over frequencies of $0.001\,\mathrm{Hz} < f < 0.1\,\mathrm{Hz}$. The red dashed line shows the result of a power-law fit to all points.

and 10^{-2} Hz, the PSDs roughly follow the Kolmogorov-like spectrum $f^{-5/3}$, even though the magnitudes are 1–2 orders of magnitude smaller than those at $R \sim 2$ au. At $10^{-2}\,\mathrm{Hz} < f < 2 \times 10^{-1}$ Hz, the spectra flatten toward a spectral index close to -1. This flattening is possibly due to instrument noise, instead of true background turbulence (Argall et al. 2017). It is necessary to consider the PSD in the frequency range well between the two break frequencies to obtain the spectral index. All cases used in this work exhibit no high-frequency spectral breaks, as shown in Table 6 of Pine et al. (2020c). We also inspect all cases to ensure that there is no low frequency break that affects our analysis. Hence, although we select a fixed frequency range to obtain the spectral index, our results are not affected by the differing spectral slopes in the energy injection range or dissipation range.

Figure 2 shows $\delta B_\parallel^2 / \delta B_\perp^2$ averaged over $0.001\,\mathrm{Hz} < f < 0.1$ Hz for all cases. $\delta B_\parallel^2 / \delta B_\perp^2$ exhibits a slight increase with R, as indicated by the power-law fit (red dashed line) of $\delta B_\parallel^2 / \delta B_\perp^2 \sim R^{-\beta}$. The fit result is $\beta \sim 0.2$, suggesting that the compressive fluctuations increase in relative importance as the solar wind propagates outward.

3.1. Radial Evolution of the Power Spectral Density and Spectral Index

To study the radial evolution of the PSDs, we divide R from 1 au to 31 au into 15 equal subranges. We calculate the time-averaged PSD in each subrange. The number of cases in each subrange varies. The number of time points also varies for each case and period. This is because the duration of each case is different and we discard data points in the cone of influence. We calculate the time-averaged PSD in the heliocentric distance range between R_{beg} and R_{end} using

$$E_{B_i}(f_j)_{R_{beg} < R_k < R_{end}}$$
$$= \frac{\sum\limits_{k: R_{beg} < R_k < R_{end}} C^k(f_j) E_{B_i}^k(f_j)}{\sum\limits_{k: R_{beg} < R_k < R_{end}} C^k(f_j)}, \qquad (6)$$

where $C^k(f_j)$ is the count of time points at frequency f_j for case k.

Since we have learned from Figure 1 that the solar wind magnetic turbulence becomes more compressible, we consider the evolution of the parallel and perpendicular fluctuations separately. Figures 3(a)–(c) show the radial evolution of $E_{B_\parallel}$, $E_{B_\perp}$, and $E_{B_{Tr}}$. The power levels decrease with R by about
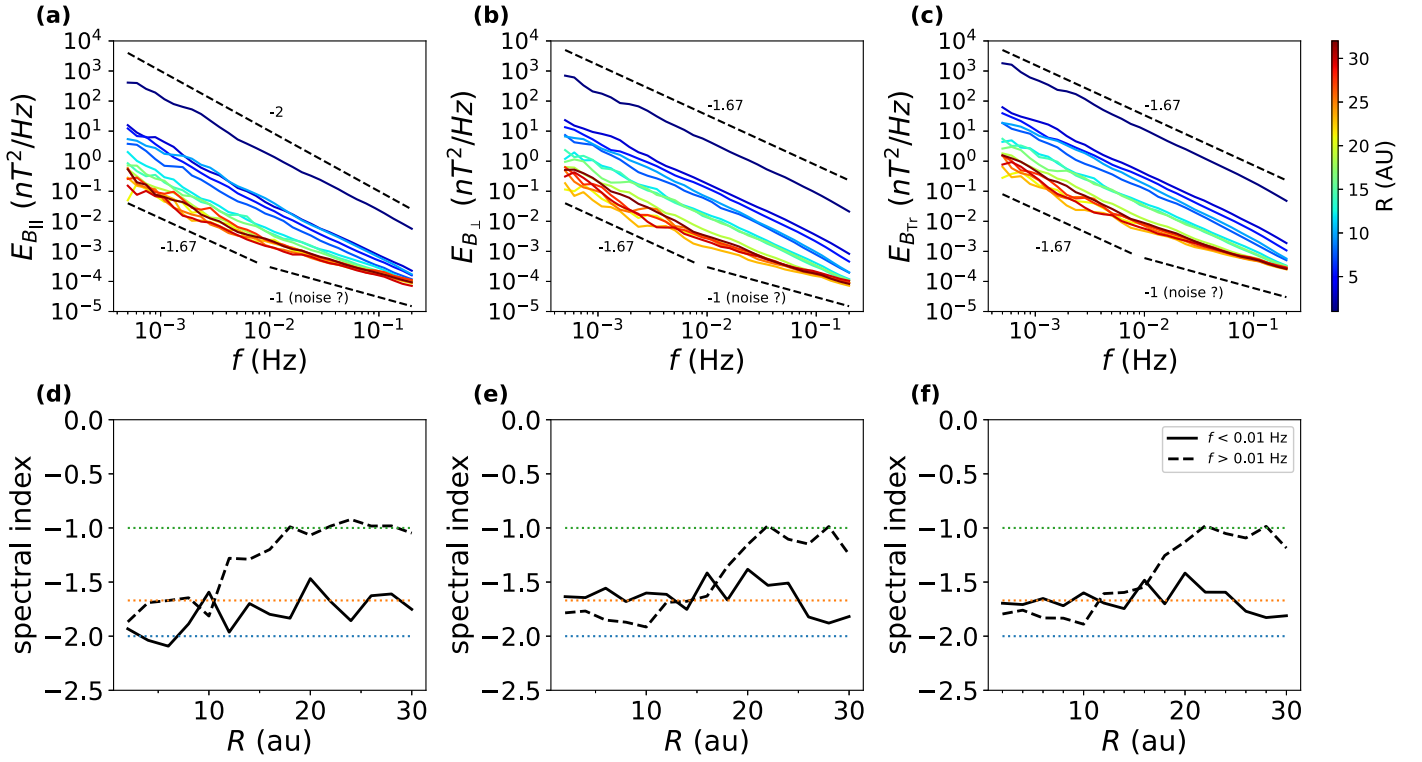
Figure 3. Radial evolution of the (a) parallel, (b) perpendicular, and (c) trace PSDs. Radial evolution of the spectral index for (d) $E_{B_\parallel}$, (e) $E_{B_\perp}$, and (f) $E_{B_{Tr}}$. The blue, orange, and green horizontal lines denote spectral indices of -2, $-5/3$, and -1, respectively.

4 orders of magnitude from ~ 1 to ~ 30 au. The PSDs at 20 au $<R<30$ au remain almost unchanged, exhibiting a double power-law shape. At frequencies 5×10^{-3} Hz $<f<10^{-2}$ Hz, all PSDs basically follow a spectrum of $f^{-5/3}$, while at frequencies 10^{-2} Hz $<f<2\times 10^{-1}$ Hz, they roughly follow a spectrum of f^{-1}. Nevertheless, there is a discrepancy between these PSDs at larger scales, and they gradually aggregate to the same value at smaller scales around 0.2 Hz.

We separately fit the PSDs at $f<10^{-2}$ Hz and $f>10^{-2}$ Hz. We then obtain the variation of the spectral index in these two regimes as a function of R (Figures 3(d)–(f)). At frequencies $f<10^{-2}$ Hz, both the power spectral indices for $E_{B_\perp}$ and $E_{B_{Tr}}$ are close to $-5/3$ over the distance range considered. The spectral index for $E_{B_\parallel}$ varies between -2 and $-5/3$ when $R<10$ au and gradually changes to $-5/3$ at $R\sim 10$ au and beyond. The evolution appears to have a different trend for frequencies $f>10^{-2}$ Hz. All spectra have a spectral index close to $-5/3$ at smaller R ($<10–15$ au). The changes of the spectral index from $-5/3$ to -1 are all gradual as R increases. The spectral indices approach -1 at $R\sim 20$ au. This systematic increase in power spectral index suggests that the fluctuations are not completely contaminated by instrument noise within 20 au. It might be a superposition of the background $f^{-5/3}$ spectrum and the instrument noise spectrum (probably in the form of f^{-1}). As the background turbulence becomes more contaminated by noise, the spectral index approaches -1.

3.2. Modeling the Radial Evolution of the Power Spectral Density at Different Scales

The spectral index variation suggests that the radial evolution of the power level might be scale dependent. Physical mechanisms may influence turbulence evolution in a wide scale range. Diagnosing the radial scaling index

α ($E_{B_i} \sim R^\alpha$) at different scales is the first step and a key to understanding the underlying physics that affects the turbulent evolution. Therefore, we study the variation of α with τ and R. First, we calculate the time-averaged PSDs for each case. Then, for each f_j, we get a scatterplot of PSD values and heliocentric distance in double logarithmic space. Due to the decrease in the decay of power, we propose a new formula to model this decrease in the power level decay rate

$$\log_{10} E_{B_i} = a_1 R^{-a_2} + a_3, \qquad (7)$$

where a_1, a_2, and a_3 are the free parameters to be fitted. This formula is just a minor revision of the WKB evolution of the turbulent power, which replaces $\langle \delta B^2 \rangle$ with $\log_{10} E_{B_i}$. We fit the scatterplot with this formula using the least-square regression method.

Figures 4(a)–(c) show the fit results at $\tau = 5$ s, 110 s, and 2000 s for $E_{B_\parallel}$, $E_{B_\perp}$, and $E_{B_{Tr}}$, respectively. At $\tau = 2000$ s, the radial scaling index is approximately constant, with a slight flattening at $R>10$ au. Next, we compare the radial decay of the power at smaller scales to the results for $\tau = 2000$ s. $E_{B_\parallel}$ and $E_{B_\perp}$ present different evolutionary features at $\tau = 110$ s. The radial scaling index is similar to that at larger scales for $E_{B_\perp}$ and $E_{B_{Tr}}$. For $E_{B_\parallel}$ at $\tau = 110$ s, the decay of power is faster at $R<5$ au and then slows down beyond 5 au. For $\tau = 5$ s, all three PSDs exhibit a much faster decrease more rapidly within 5 au and flatten at $R>20$ au.

We use the slope of the fitting curves in Figures 4(a)–(c) to estimate the local radial scaling index. Figures 4(d)–(f) show the distributions of the estimated radial scaling index in τ–R space for $E_{B_\parallel}$, $E_{B_\perp}$, and $E_{B_{Tr}}$. Looking at the distribution of $E_{B_\parallel}$, the radial decay of power at smaller scales preferentially slows down at $R>2$ au. For $E_{B_\perp}$ and $E_{B_{Tr}}$, the variation of the radial scaling index seems to be period independent at $\tau>100$ s.
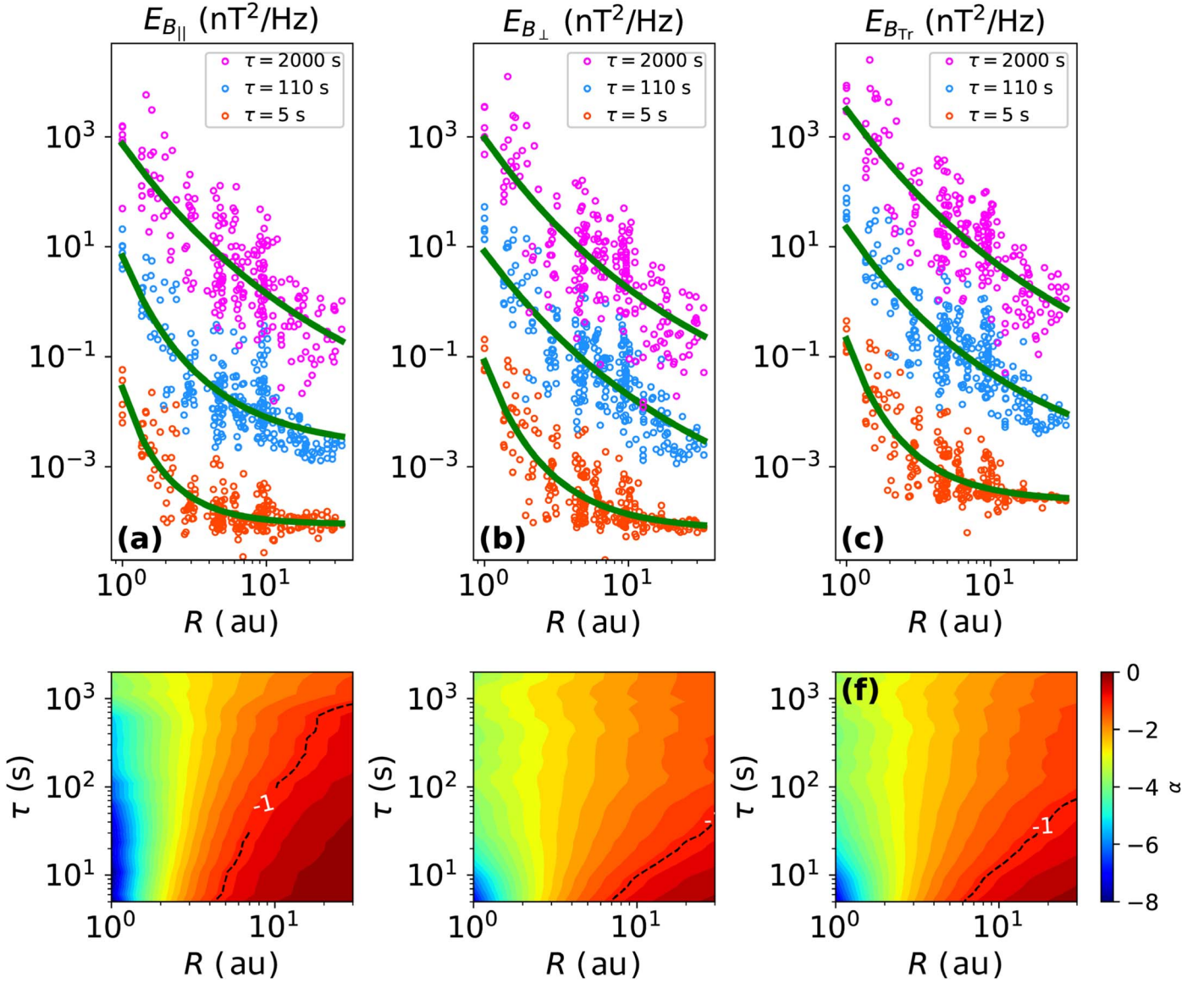
Figure 4. (a)–(c) Time-averaged PSDs at three periods (5 s, 110 s, and 2000 s) for all cases considered. The dark green solid lines denote the fit results for each period. (d)–(f) Distributions of the estimated local radial scaling index α for $E_{B_\parallel}$, $E_{B_\perp}$, and $E_{B_{Tr}}$, respectively. The dashed line marks the contour level of -1, around and below which the PSDs are potentially contaminated by noise.

At $\tau < 100$ s, the power at smaller scales also flattens as R increases. At $R < 3$ au, the decay of power at small scales dramatically steepens with decreasing R.

4. Radial Evolution of the Magnetic Turbulence Anisotropy in the Outer Heliosphere

Figures 1(f) and (g) show that the period–time spectrograms of the propagation angle have different features at $R \sim 2$ au and $R \sim 30$ au. Hence, we explore how this transformation occurs and at what distance it occurs.

4.1. Radial Evolution of the Propagation Angle Distribution

We divide R from 1 to 31 au into 15 equal subranges. We allocate the cases into these distance ranges according to the position of Voyager 2. For each distance range and each period, we bin the subdata set into 30 bins of $\theta(\boldsymbol{k}, \boldsymbol{B}_0)$ in the range from $0°$ to $90°$. We then calculate the 1D probability density function (PDF) of $\theta(\boldsymbol{k}, \boldsymbol{B}_0)$ at each period and in each distance

range. The PDFs in six different R ranges are shown in Figure 5.

Figure 5 shows that a transition of the $\theta(\boldsymbol{k}, \boldsymbol{B}_0)$ distribution occurs in the R range between 5 and 10 au. For $R < 5$ au, they exhibit a characteristic transition of "quasi perpendicular" to "quasi parallel" to "quasi perpendicular" from larger scales to smaller scales. The transition periods are roughly at 500 and 10 s, respectively. The first transition, from quasi perpendicular to quasi parallel, is sharp, while the second is a more gradual transition. For 5 au $< R <$ 7 au and for periods 10 s $< \tau <$ 500 s, the PDF increases for propagation angles greater than $30°$ while the most probable angle is still quasi parallel. At 7 au $< R <$ 9 au, the most probable propagation angle is quasi perpendicular. As the solar wind continues to travel outward, the probability gradually decreases for propagation angles less than $30°$. At $R > 10$ au, the propagation angle is greater than $30°$ for almost all periods.

The distribution of $\theta(\boldsymbol{k}, \boldsymbol{B}_0)$ at 10 s $< \tau <$ 500 s agrees with Figure 7 of Pine et al. (2020d). However, there are more events
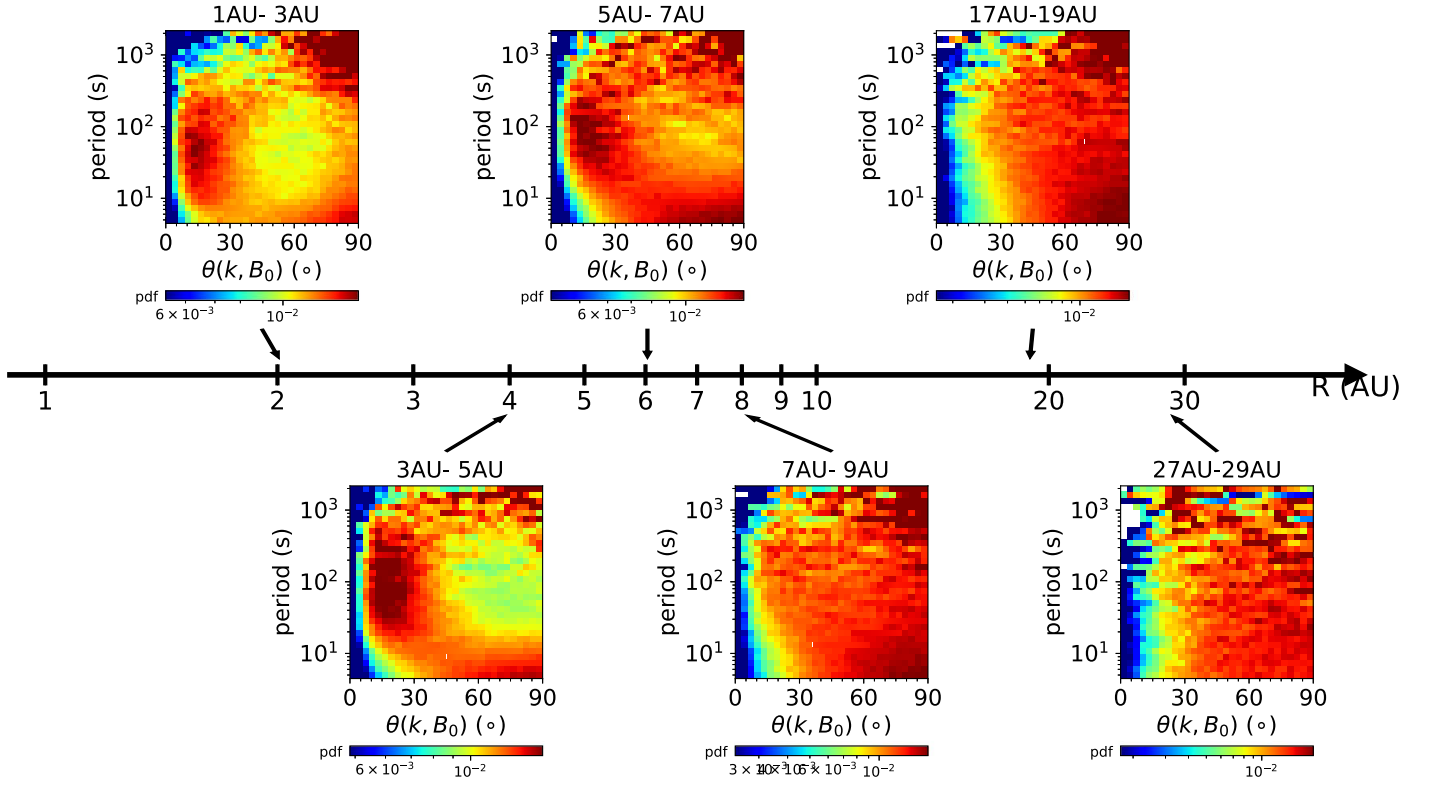
Figure 5. PDF of the propagation angle $\theta(\boldsymbol{k}, \boldsymbol{B}_0)$ in the heliocentric distance range from 1 to 30 au. The PDF is calculated at each period and in each distance subrange.

with $\theta(\boldsymbol{k}, \boldsymbol{B}_0) \lesssim 30°$ at $R < 7$ au and $\theta(\boldsymbol{k}, \boldsymbol{B}_0) \gtrsim 20°$ at $R > 10$ au in Figure 7 of Pine et al. (2020d). This indicates that $\theta(\boldsymbol{k}, \boldsymbol{B}_0)$ concentrates around smaller angles at $R < 7$ au and spreads over angles greater than $30°$ at $R > 10$ au, consistent with our result shown in Figure 5. In addition, the differences between our figures and Figures 5 and 7 of Pine et al. (2020d) are potentially due to the choice of coordinate system (using local mean-field coordinates versus using global mean-field coordinates).

4.2. Average Power Spectral Densities for Different Propagation Angles

There is a clear correspondence between $E_{\mathrm{B}_\parallel}(\tau_\mathrm{j}, t_\mathrm{n})$ and $\theta(\boldsymbol{k}, \boldsymbol{B}_0)(\tau_\mathrm{j}, t_\mathrm{n})$ at t_n and τ_j based on our calculation. We divide the heliocentric distances from 1 to 25 au into five nonoverlapping ranges and regarding all points at $R > 25$ au as another heliocentric distance range. In a given R range, we consider all cases for which the position of Voyager 2 is within it. For each period, we bin the PSDs into 30 bins of $\theta(\boldsymbol{k}, \boldsymbol{B}_0)$ in the range from $0°$ to $90°$. We then calculate the average PSD in each bin. The average PSDs in three R ranges are shown in Figure 6. Within each R range, the PSDs have no obvious radial evolution (not shown here). For each period, $E_{\mathrm{B}_\parallel}$ sharply increases with propagation angle when $\theta(\boldsymbol{k}, \boldsymbol{B}_0) < 20°$. It is followed by a mild increase of PSD with propagation angle when $\theta(\boldsymbol{k}, \boldsymbol{B}_0) > 20°$.

The distributions of $E_{\mathrm{B}_\perp}$ is more isotropic compared to $E_{\mathrm{B}_\parallel}$. At 1 au $< R < 5$ au, $E_{\mathrm{B}_\perp}$ increases with $\theta(\boldsymbol{k}, \boldsymbol{B}_0)$ for periods $\tau < 50$ s but decreases with $\theta(\boldsymbol{k}, \boldsymbol{B}_0)$ for periods $\tau > 50$ s. At $R > 5$ au, the distribution of $E_{\mathrm{B}_\perp}$ increases with $\theta(\boldsymbol{k}, \boldsymbol{B}_0)$ at $\tau > 50$ s. Such an increase is mainly due to the enhancement of

power for $\theta(\boldsymbol{k}, \boldsymbol{B}_0) < 20°$. We note that $E_{\mathrm{B}_\perp}$ is almost angular independent when $\theta(\boldsymbol{k}, \boldsymbol{B}_0) > 30°$.

The variation of $E_{\mathrm{B}_\parallel}$ with $\theta(\boldsymbol{k}, \boldsymbol{B}_0) < 20°$ is controlled by the divergence-free condition of magnetic field fluctuations, $\boldsymbol{k} \cdot \delta\boldsymbol{B} = 0$. This leads to the rapid decrease of $E_{\mathrm{B}_\parallel}$ when $\theta(\boldsymbol{k}, \boldsymbol{B}_0)$ tends to zero. The finite $E_{\mathrm{B}_\parallel}$ reveals the weakly compressive nature of the quasi-parallel mode and the compressibility increases with $\theta(\boldsymbol{k}, \boldsymbol{B}_0)$, given that $E_{\mathrm{B}_\perp}$ is more isotropic as per Figures 6(b), (e), and (h).

4.3. Power Spectral Indices for Different Propagation Angles

In this subsection, we study the angular dependence of the power spectral index for periods 100 s $< \tau < 2000$ s and 5 s $< \tau < 100$ s. First, we coarsen the angular bins into three nonoverlapping $30°$ intervals to clarify the results. Next, we calculate the averaged PSD for each bin. We then fit the PSDs in these two period ranges. The results are shown in Figure 7.

The indices have no systematic angular dependence and no systematic radial evolution in the range of 100 s $< \tau < 2000$ s. In this period range, the indices vary between -2.0 and -1.67 for $E_{\mathrm{B}_\parallel}$, while the indices for $E_{\mathrm{B}_\perp}$ and $E_{\mathrm{B}_{\mathrm{Tr}}}$ are concentrated around -1.67. The indices for PSDs at distances between 20 au and 25 au show a clear angular dependence. The power spectral index decreases with propagation angle. However, it is unclear what causes this angular dependence of the indices in this distance range.

The angular dependence of the power spectral indices shows a clear radial evolution when 5 s $< \tau < 100$ s. In the heliocentric distance range of $R < 10$ au, the spectral index decreases with propagation angle while the power spectral index increases with propagation angle for $R > 15$ au. In the transition distance range between 10 and 15 au, the index
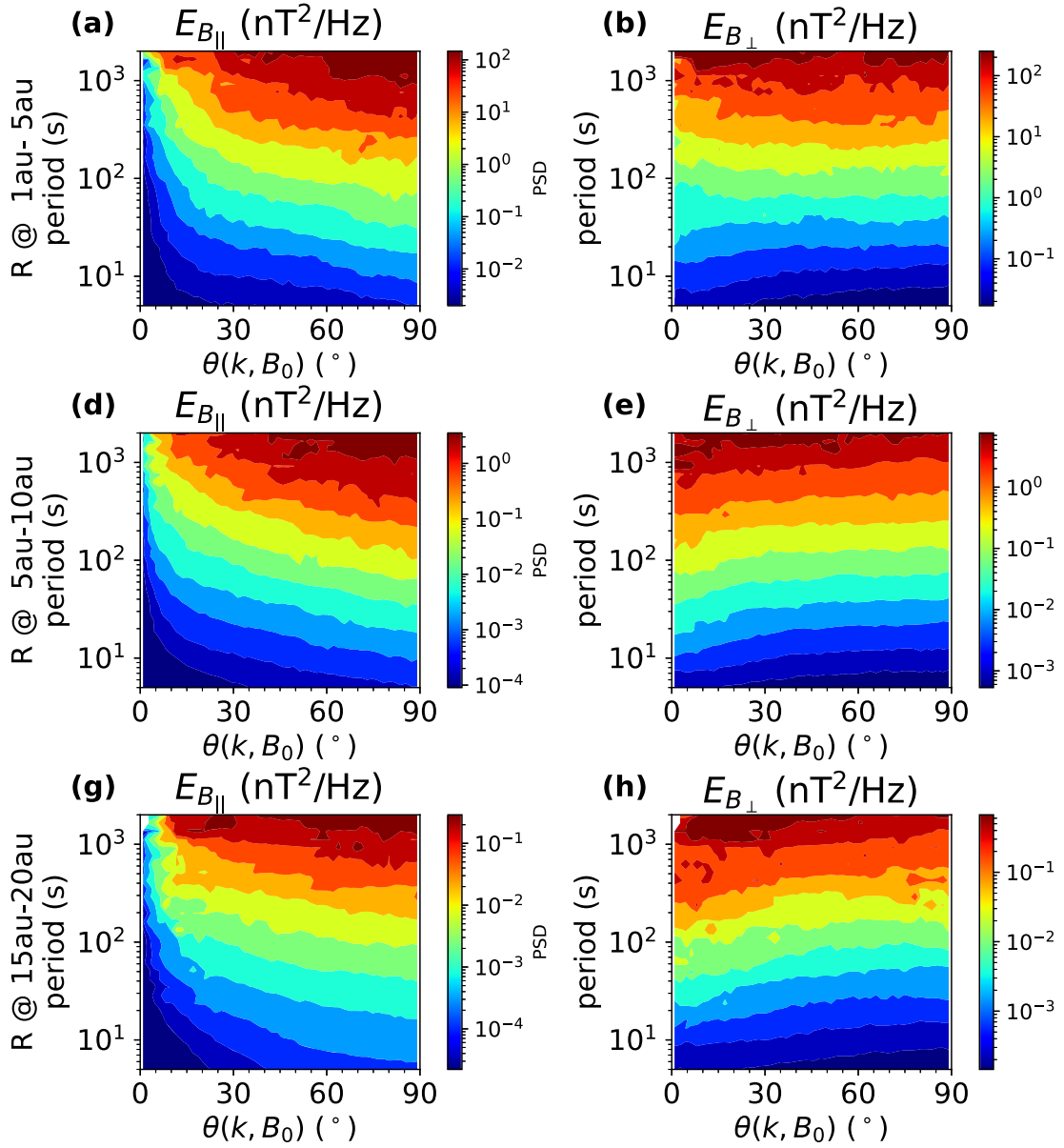
Figure 6. PSDs of magnetic field fluctuations, $E_{B_\parallel}$ (left column), and $E_{B_\perp}$ (right column) for different propagation angles $\theta(\mathbf{k}, \mathbf{B_0})$ and different periods τ, which are averaged over three heliocentric distance ranges (top: 1 au $< R <$ 5 au; middle: 5 au $< R <$ 10 au; and bottom: 15 au $< R <$ 20 au).

values peak within $30° < \theta(\mathbf{k}, \mathbf{B_0}) < 60°$. The average index values increase with heliocentric distance, which is consistent with Figure 3.

5. Radial Evolution of the Power Spectra from 0.1 to 30 au

Measurements from PSP show that the power spectral index for solar wind plasma turbulence evolves radially in the inner heliosphere (Chen et al. 2020). Here, we extend the picture of the evolution of solar wind turbulence to the outer heliosphere to around 30 au (Figure 8). The overall power spectra decrease by 3 orders of magnitude from 0.1 to 1 au and 4 orders of magnitude from 1 to 30 au. The break frequency between the energy-containing range ($\sim f^{-1}$ spectrum at low frequencies) and the inertial range shifts to lower frequencies with increasing distance. The typical proton cyclotron frequency is around 2×10^{-3} Hz at $R \sim 30$ au. However, there is no break frequency between the inertial range and the kinetic range that

steepens the spectrum, which would be anticipated based on dissipation and/or dispersion of the fluctuations at small scales. Instead, the spectrum still follows a Kolmogorov-like scaling until the spectrum flattens. This is probably just an instrumental problem and not a physical property of the turbulence.

6. Summary and Discussion

In this paper, we study the radial evolution of solar wind turbulence and the evolution of the turbulence anisotropy in the outer heliosphere. The inertial-range $E_{B_\perp}$ and $E_{B_{Tr}}$ maintain an index close to $-5/3$ until $R \sim 30$ au. The spectral profile of $E_{B_\parallel}$ is steeper from 1 to 10 au, and the spectral index increases to $-5/3$ beyond 10 au. These results are valid for frequencies $f < 0.1$ Hz in the Voyager 2 measurements, and exclusively when the fluctuations are not dominated by instrument noise. Both power spectral indices of $E_{B_\perp}$ and $E_{B_{Tr}}$ exhibit a gradual transition from $-5/3$ to -1. For a spectrum with an index
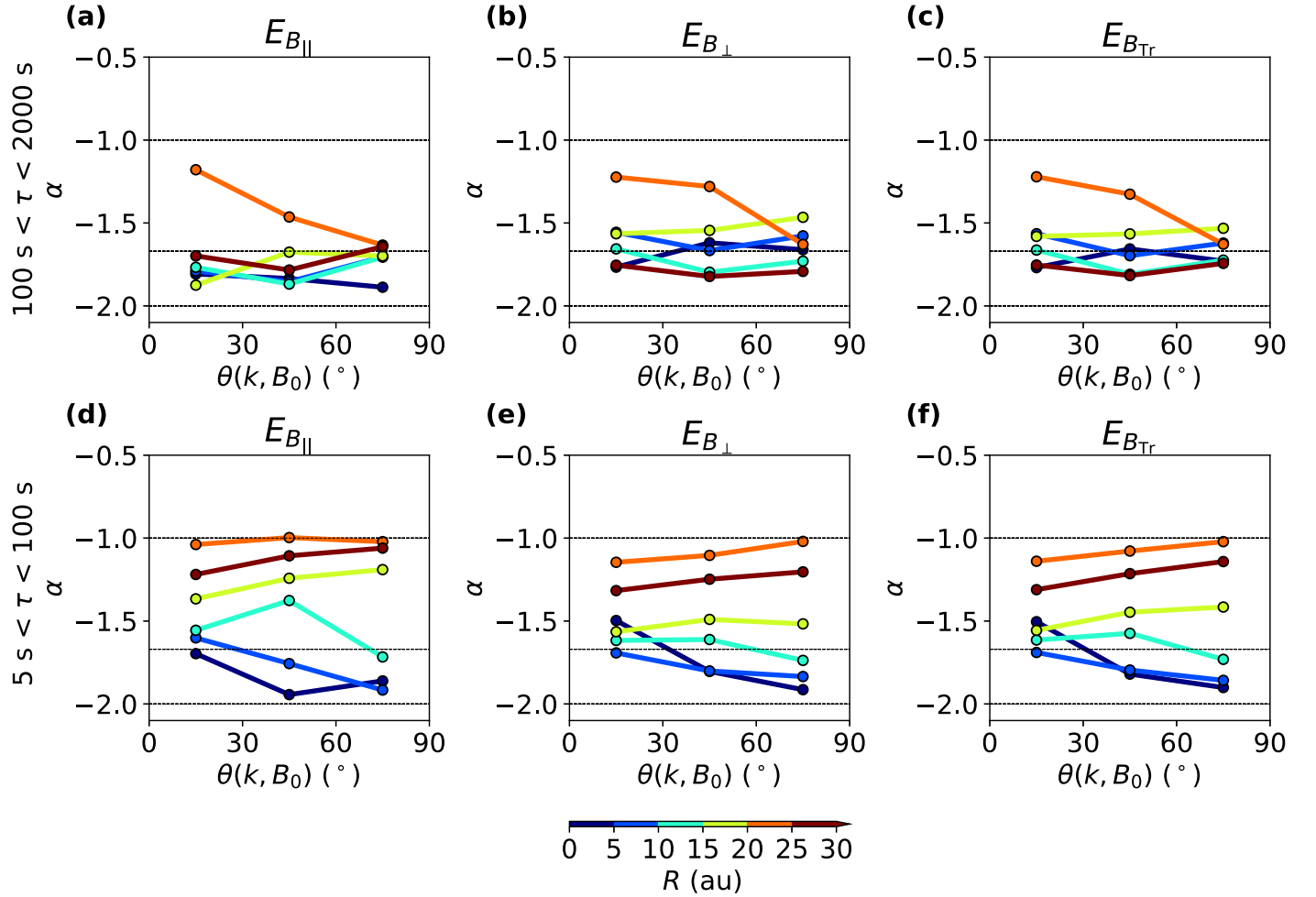
Figure 7. Power spectral index as a function of propagation angle $\theta(\boldsymbol{k}, \boldsymbol{B_0})$ in different heliocentric distance ranges. (a)–(c) Power spectral indices for (a) $E_{B_\parallel}$, (b) $E_{B_\perp}$, and (c) $E_{B_{Tr}}$ in the period range of $100\ \text{s} < \tau < 2000\ \text{s}$. (d)–(f) Power spectral indices for (d) $E_{B_\parallel}$, (e) $E_{B_\perp}$, and (f) $E_{B_{Tr}}$ in the period range of $5\ \text{s} < \tau < 100\ \text{s}$.

between $-5/3$ and -1 in the range of $10\ \text{au} < R < 20\ \text{au}$, our results suggest that the observed spectrum is a superposition of true background turbulence and instrument noise. The noise spectrum increasingly dominates the observed spectrum as the solar wind propagates outward. Nevertheless, studying the turbulence properties at lower frequencies is still possible, even if noise contaminates the measurements at higher frequencies. We propose to model the radial scaling of the PSD by a power-law relation between $\log_{10}E_{B_i}$ and R. The radial scaling is roughly period independent at $100\ \text{s} < \tau < 2000\ \text{s}$. This model represents well the slowdown of power decay beyond 10 au. However, we still need a physical explanation for this modeled behavior.

The anisotropy turbulence evolves significantly in the range between 5 and 10 au. At $R < 5$ au, the fluctuations are primarily quasi-parallel propagating ($\theta(\boldsymbol{k}, \boldsymbol{B_0}) < 30°$) for periods $10\ \text{s} < \tau < 500\ \text{s}$. In the range of $5\ \text{au} < R < 7\ \text{au}$, quasi-perpendicular-propagating fluctuations become more distinct, but still, quasi-parallel fluctuations dominate. From $R \sim 7$ au, obliquely propagating fluctuations ($\theta(\boldsymbol{k}, \boldsymbol{B_0}) > 30°$) become the major component and most are quasi-perpendicular propagating ($\theta(\boldsymbol{k}, \boldsymbol{B_0}) > 60°$). $E_{B_\perp}$ at periods $100\ \text{s} < \tau < 2000\ \text{s}$ increases with $\theta(\boldsymbol{k}, \boldsymbol{B_0})$ within 5 au. Interestingly, we observe an enhancement in $E_{B_\perp}$ at smaller propagation angles $\theta(\boldsymbol{k}, \boldsymbol{B_0}) < 20°$ beyond 5 au. This results in the PSD decreasing with $\theta(\boldsymbol{k}, \boldsymbol{B_0})$ at further distances.

The choice of using a local rather than global mean field does not have a significant impact on our anisotropy results. We find that choosing a global mean magnetic field only slightly modifies the spectral index of $E_{B_\parallel}$ within $R < 10$ au to -1.65. When using the global mean field, the PDF of $\theta(\boldsymbol{k}, \boldsymbol{B_0})$ at $1\ \text{au} < R < 3\ \text{au}$ does not concentrate around quasi-parallel directions for $10\ \text{s} < \tau < 500\ \text{s}$ (not shown here). Previous work (Cho & Vishniac 2000; Luo & Wu 2010; Chen et al. 2011b) notes that only by choosing the local mean field can the spectral and variance anisotropies be detected in the inertial range.

6.1. The f^{-1} Instrument Noise

Previous studies (Argall et al. 2017; Hollick et al. 2018; Pine et al. 2020a) notice the unique f^{-1} spectrum in the frequency range $0.01\ \text{Hz} < f < 0.2\ \text{Hz}$. These authors interpret the f^{-1} spectrum as due to instrument noise. Argall et al. (2017) argue that the f^{-1} spectrum exhibits a common power level which is about $5 \times 10^{-3}\ \text{nT}^2\ \text{Hz}^{-1}$ at 0.01 Hz. If it is scaled to higher frequencies, the power levels are comparable with the preflight instrument noise spectrum of the magnetometer. Hollick et al. (2018) suggest that, although physical processes can produce an f^{-1} spectrum, these processes are unlikely to act in this frequency range. We agree that it is likely that this spectrum is due to instrument noise.
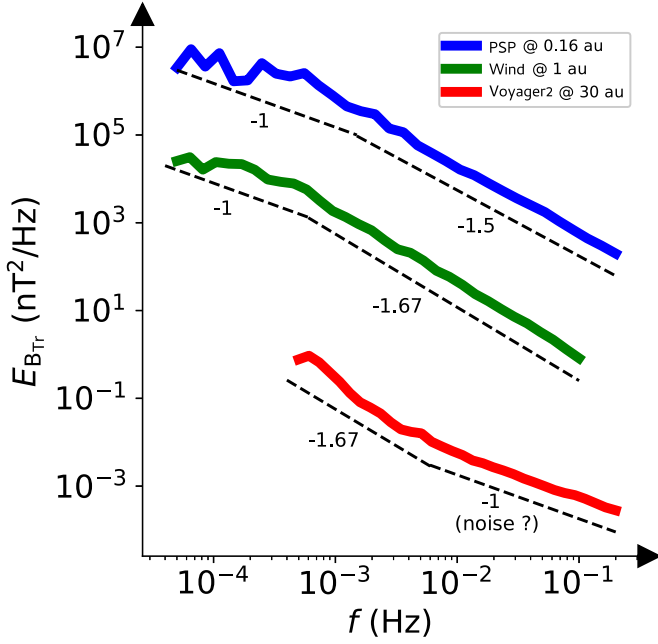
Figure 8. Typical trace power spectra of magnetic field turbulence at three distances observed by PSP at 0.16 au (blue), WIND at 1 au (green), and Voyager 2 at 30 au (red). The black dashed lines represent the power-law fits of the spectra at each period range with the power spectral index values marked alongside.

However, we express some doubts about comparing the observed noise level and the calibrated preflight noise level. The observed spectrum has a power level of 5×10^{-3} nT^2 Hz^{-1} at 0.01 Hz. Thus, the scaled power level is 5×10^{-4} nT^2 Hz^{-1} at 0.1 Hz. This value is an order of magnitude greater than the preflight noise spectral level at this frequency, 5×10^{-5} nT^2 Hz^{-1} (see Figure 7 of Behannon et al. 1977). The power levels are not entirely saturated at frequencies $f \gtrsim 0.01$ Hz. PSDs at different distances have minor discrepancies, although they converge to nearly the same value at $f \lesssim 0.2$ Hz. Based on these results, we cannot fully rule out the contribution of background turbulent fluctuations to the observed spectra at $f \gtrsim 0.01$ Hz.

6.2. Activity of Compressive Fluctuations in the Energy Transport

Chen (2016) argues that a passive scalar field possesses the same spectrum as an advecting field. Observations at $R \sim 1$ au (Chen et al. 2011a) show that both the density and compressive magnetic fluctuations have an $f^{-5/3}$ spectrum, being interpreted as compressive fluctuations being passively advected by Alfvénic turbulence (Goldreich & Sridhar 1997; Schekochihin et al. 2009). In our work, we find that for frequencies $f < 0.01$ Hz, $E_{B_\parallel}$ is steeper than $E_{B_\perp}$ in the distance range of 1 au $< R <$ 10 au, although the perpendicular fluctuations are dominant. However, the spectral indices are approximately the same (close to $-5/3$) at 10 au $< R <$ 30 au for these two spectra.

The nature and origin of compressive fluctuations in the outer heliosphere are issues yet to be fully understood. Some fluctuations at hourly scales or less have been identified as pressure-balanced structures (PBSs), mainly based on the anticorrelation between thermal pressure and magnetic pressure (Burlaga 1968; Roberts et al. 1987; Burlaga et al. 1990). The PBSs in the outer heliosphere progressively build up in the

solar wind (Vellante & Lazarus 1987; Roberts 1990), which is consistent with the prediction for the "pseudosound" pressure-balanced variation in the context of nearly incompressible theory (Montgomery et al. 1987; Roberts 1990; Zank & Matthaeus 1992). In our study, $E_{B_\parallel}$ within 10 au possesses a spectral index close to -2, suggesting that PBSs dominate the compressive fluctuations because large jumps in the parallel magnetic field result in a -2 spectrum (Burlaga & Klein 1986; Goldreich & Sridhar 1997). Corotating interaction regions (CIRs) are the most common large-scale structures in the solar wind within 8 au, naturally dividing the solar wind into unshocked/pristine and shocked/compressed regions. As a CIR propagates outward, the CIR-associated shock pairs expand, enlarging the compression region. At 8 au $< R <$ 12 au, CIRs often merge and interpenetrate, leading to the formation of merged interaction regions (MIRs) and corotating pressure enhancements (CPEs) without shock pairs at even greater distances (Gazis et al. 1999). The presence and evolution of MIRs and CPEs indicate that the compressed solar wind diffuses and occupies a larger heliospheric volume. This process provides a potential source for the compressive fluctuations at $R > 10$ au, possibly consisting of fast magnetosonic waves and PBSs (Tu & Marsch 1994). This interpretation is consistent with our finding that $E_{B_\parallel}$ holds a spectral index of $-5/3$, different from the PBS-dominated interval at $R < 10$ au. Future work requires a detailed examination of the nature of the compressive fluctuations depending on heliocentric distance (e.g., using the mode decomposition method developed by Zank et al. 2023).

Our results suggest that compressive fluctuations are active in the outer heliosphere beyond 10 au. Howes et al. (2012) suggest that the nature of the compressive fluctuations is mostly slow mode–like for solar wind turbulence, although this is under debate (e.g., Zhao et al. 2022). The nonlinear interaction time between counterpropagating Alfvén wave packets (δz_A), τ_{AA}, is $\sim (k_\perp \delta z_A)^{-1}$, while the corresponding interaction time between a slow wave packet (δz_S) and an Alfvén wave packet, τ_{SA}, is $\sim (k_\parallel \delta z_S)^{-1}$, where $\delta z_M = \delta V + \delta B / \sqrt{\mu_0 \rho_0}$ (M = A, S), δV is the fluctuation of the plasma bulk velocity, δB is the magnetic field fluctuation, ρ_0 is the average mass density, and μ_0 is the permeability of vacuum. The ratio of these two characteristic times is $\tau_{AA}/\tau_{SA} \sim (\delta z_S/\delta z_A) \cdot (k_\parallel/k_\perp) \sim (\delta B_\parallel/\delta B_\perp) \cdot (k_\parallel/k_\perp) \sim (\delta B_\parallel/\delta B_\perp)^{8/3}$. This last derivation has used the relation between the wavevector anisotropy and the spectral anisotropy, which is $(k_\parallel/k_\perp) = (\delta B_\parallel/\delta B_\perp)^{5/3}$ based on critical-balance theory (Chen et al. 2010b). If compressive fluctuations are enslaved to Alfvénic fluctuations, this ratio should be close to zero, certainly smaller than 0.1. Based on our results, at 1 au $< R <$ 10 au, $\delta B_\parallel/\delta B_\perp \approx 0.3$, so that τ_{AA}/τ_{SA} is about 0.04. At 10 au $< R <$ 30 au, $\delta B_\parallel/\delta B_\perp \approx 0.65$, and τ_{AA}/τ_{SA} is about 0.31. Throughout the distance range from 10 to 30 au, τ_{SA} is comparable to τ_{AA}. This suggests that the compressive fluctuations may actively participate in the turbulent cascade process. However, the spectral index for $E_{B_\parallel}$ is close to that for $E_{B_\perp}$. We do not yet know the quantitative dependence of the spectral shape on this ratio. A future model needs to be developed concerning the relation between the spectral index and τ_{AA}/τ_{SA}.

6.3. Wavevector Anisotropy of Inertial-range Turbulence

The propagation angle $\theta(\boldsymbol{k}, \boldsymbol{B_0})$ PDFs serve as a hint for the energy cascade direction in wavevector space. For 1 au $< R < 5$ au, the most probable $\theta(\boldsymbol{k}, \boldsymbol{B_0})$ transits from less than

(a)

(b)
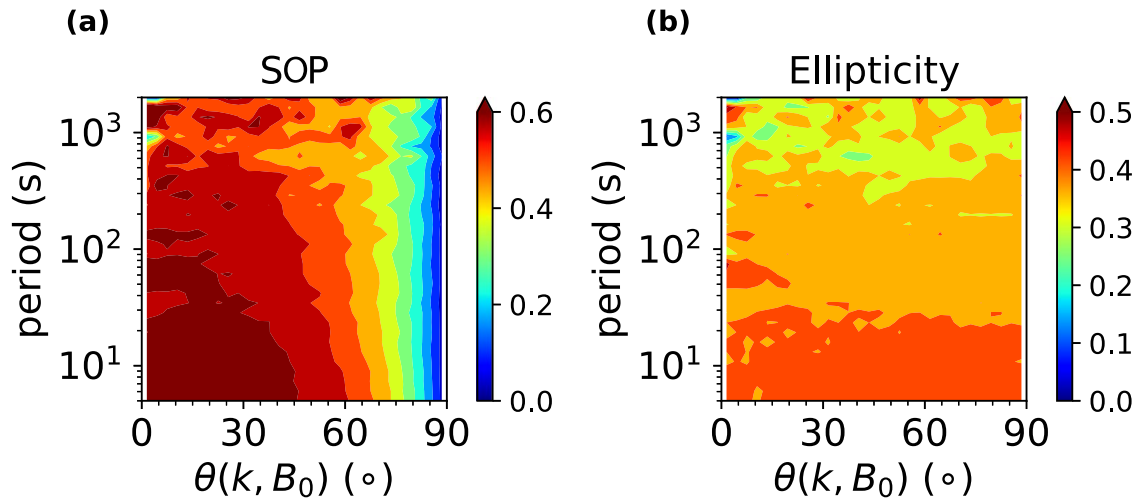
Figure 9. (a) Magnitude of the SOP and (b) ellipticity as a function of period and propagation angle at heliocentric distances of 10 au $< R <$ 15 au.

$30°$ toward greater than $30°$ as the period decreases. The transition tendency implies that the turbulent cascade process transports magnetic field energy toward larger $k_\perp$. This feature is similar to the nature of turbulence observed in the inner heliosphere (He et al. 2013; Zhu et al. 2020). Whether the cascade process complies with critical-balance theory or 2D slab superposition theory (Zank et al. 2020) needs further investigation. Figure 5 shows that $\theta(\boldsymbol{k}, \boldsymbol{B_0})$ is distributed over angular ranges between $30°$ and $90°$ for periods $5\,\mathrm{s} \lesssim \tau \lesssim 10\,\mathrm{s}$. We speculate that the turbulent fluctuations consist of a mixture of oblique Alfvén/ion–cyclotron waves and quasi-perpendicular kinetic Alfvén waves at this scale range. To study the nature of the turbulent fluctuations, we need a further comparison with linear Vlasov theory and observations regarding the dispersion relation and the polarization properties of the fluctuations. However, such work is beyond the scope of the effort here.

An interesting result lies in the transition of the $\theta(\boldsymbol{k}, \boldsymbol{B_0})$ distribution from 5 to 10 au for periods of $10\,\mathrm{s} < \tau < 500\,\mathrm{s}$. As the solar wind flows outward, fluctuations associated with $\theta(\boldsymbol{k}, \boldsymbol{B_0})$ greater than $30°$ progressively dominate the quasi-parallel-propagating fluctuations. Oughton & Matthaeus (2005) integrate two primary phenomenological theories for turbulence anisotropy, namely the slab + 2D (Matthaeus et al. 1990; Zank & Matthaeus 1992, 1993) and critical-balance (Goldreich & Sridhar 1995) scenarios. They propose that the fluctuations can be treated as either quasi-parallel wave-like or quasi-2D turbulent. The type of fluctuations is determined by the ratio between the nonlinear and Alfvén times. In Fourier space, the turbulent fluctuations have a shorter nonlinear timescale and fill a larger $k_\perp$ (larger propagation angle) region relative to the critical-balance ridge. Inspired by the idea of Oughton & Matthaeus (2005), we propose that the solar wind turbulence becomes more close to hydrodynamic fluid turbulence as the solar wind evolves from 5 to 10 au. Another possible evidence is that the spectra in the parallel and perpendicular directions follow a Kolmogorov $-5/3$ spectrum beyond 10 au.

6.4. Turbulent Energy Anisotropy of Inertial-range Turbulence

The power spectral anisotropies reveal a radial evolution, especially from R inside to outside 5 au (Figure 6). Particularly, in the period range from 100 to 2000 s, $E_{\mathrm{B_\perp}}(f)$ increases with

$\theta(\boldsymbol{k}, \boldsymbol{B_0})$ at 1 au $< R <$ 5 au, whereas quasi-parallel-propagating fluctuations possess greater energies at 5 au $< R <$ 10 au. This evolution indicates that a different mechanism influences the energy cascade process for solar wind turbulence at $R > 5$ au.

We propose that the $E_{\mathrm{B_\perp}}$ enhancement associated with quasi-parallel-propagating fluctuations beyond 5 au could be due to energy injection originating from PUIs. The hydrogen ionization cavity reaches out to ~ 8 au (Zank 1999; Zank et al. 2017). Beyond this distance, the amount of PUIs is large enough to influence the solar wind dynamics. The newly generated PUIs introduce a superthermal energy source to the thermal solar wind plasma. This kind of energy source can excite quasi-parallel circularly polarized waves (Lee & Ip 1987). Observational evidence (Argall et al. 2017; Hollick et al. 2018) shows the prevalence of cyclotron waves created by PUIs, suggesting that PUIs have a prolonged influence on the solar wind plasma.

We show the angle- and period-dependent distributions of the sense of polarization (SOP) and ellipticity in Figure 9. The definitions of these quantities are summarized in the Appendix. The SOP is inversely correlated with $\theta(\boldsymbol{k}, \boldsymbol{B_0})$. This indicates that the orthogonal components have a higher coherence at small propagation angles, and thus the quasi-parallel-propagating fluctuations are more wave-like (He et al. 2022; Zhu et al. 2023). At small propagation angles, the SOP is slightly greater at $\tau < 100$ s than at $\tau > 100$ s. The ellipticity distribution is isotropic at a constant period. The ellipticity increases with decreasing period, which is in contrast to observations near the Sun (Zhu et al. 2020). Hence, the enhancement of $E_{\mathrm{B_\perp}}$ in parallel-propagating fluctuations is accompanied by fluctuations with high coherence. Based on these two findings, we speculate that the fluctuations with quasi-parallel propagation are due to energy injection provided by PUIs.

The variance anisotropy is insufficient to infer the genuine spectral anisotropy (Chen et al. 2010a; Oughton et al. 2015; Wang et al. 2020), since the spacecraft only measures a reduced spectrum. Instead of analyzing the spectral anisotropy based on the variance anisotropy, we present the PSD distribution as a function of the propagation angle obtained by the SVD technique. This determination of the propagation angle is more directly related to the relative importance of the parallel and perpendicular fluctuations. A smaller propagation angle

suggests that the perpendicular magnetic field fluctuations are more dominant. Hence, the PSD distribution reflects the magnetic power associated with different compressibilities at a constant period.

Nevertheless, the variance anisotropy still provides information about the energy partition between the slab and 2D components (Bieber et al. 1996; Hamilton et al. 2008). Resolving the spectral anisotropy based on the measured time series is essential for understanding the nature of the turbulence and the evolution of turbulence, for example, in transport models (Adhikari et al. 2017; Zank et al. 2017, 2018). Different methods (Adhikari et al. 2017; Bandyopadhyay & McComas 2021) have been proposed to quantify the energy ratio of the slab and 2D components. However, determining this ratio is beyond the scope of our work. An alternative approach is to employ a method akin to tomographic inversion. This involves studying the variation of 1D reduced spectra with respect to sampling angles, allowing the measurement of turbulence power spectra in multidimensional wavenumber space (He et al. 2013). This method enables a direct comparison of the ratio between the slab and 2D components. A method resembling tomographic inversion has previously been applied in the analysis of turbulence measurements by the Helios and Wind spacecraft within the inner heliosphere and upstream of the Earth, successfully reconstructing the anisotropic distribution features of turbulence power spectra in wavenumber space (He et al. 2013; Yan et al. 2016).

Turbulence transport models (Isenberg et al. 2003, 2010; Usmanov et al. 2016; Zank et al. 2018) typically assume the wave energy is quickly smoothed over the inertial-range spectrum. However, these models do not typically address the influence of the PUI source on turbulence anisotropy. The power spectra we study here do not show a wave-like signature in the form of a local power spectral enhancement. Therefore, the power spectral anisotropy may not be affected by these wave fluctuations. Our work provides an observational constraint on the anisotropy of PUI-mediated turbulence in the outer heliosphere.

Acknowledgments

Appendix
Sense of Polarization and Ellipticity

We transform the magnetic field wavelet spectra $\tilde{\boldsymbol{B}} = (\tilde{B}_R, \tilde{B}_T, \tilde{B}_N)$ in RTN coordinates to local mean magnetic field coordinates through

$$\tilde{B}_{\parallel} = \tilde{\boldsymbol{B}} \cdot \boldsymbol{e}_{\parallel},$$
$$\tilde{B}_{\perp 1} = \tilde{\boldsymbol{B}} \cdot \boldsymbol{e}_{\perp 1},$$
$$\tilde{B}_{\perp 2} = \tilde{\boldsymbol{B}} \cdot \boldsymbol{e}_{\perp 2}, \qquad \text{(A1)}$$

where $\boldsymbol{e}_{\parallel}$, $\boldsymbol{e}_{\perp 1}$, and $\boldsymbol{e}_{\perp 2}$ are the unit vectors of the mean-field coordinates in RTN coordinates. We define the SOP with respect to the local mean magnetic field direction as

$$\text{SoP} = \frac{2 \, \text{Im}\left(\tilde{B}_{\perp 1} \tilde{B}_{\perp 2}^{*}\right)}{|\tilde{B}_{\perp 1}|^2 + |\tilde{B}_{\perp 2}|^2}. \qquad \text{(A2)}$$

SOP varies in the range of -1 and $+1$.

The SVD technique yields three singular values, with the two largest values representing the axes of the fluctuation ellipse orthogonal to the minimum singular vector direction. Hence, the ellipticity is defined as the ratio of the median and maximum singular values.

ORCID iDs

Xingyu Zhu ⓘ https://orcid.org/0000-0002-1541-6397
Jiansen He ⓘ https://orcid.org/0000-0001-8179-417X
Gary P. Zank ⓘ https://orcid.org/0000-0002-4642-6192
Daniel Verscharen ⓘ https://orcid.org/0000-0002-0497-1096
Ling-Ling Zhao ⓘ https://orcid.org/0000-0002-4299-0490
Die Duan ⓘ https://orcid.org/0000-0002-6300-6800
Rong Lin ⓘ https://orcid.org/0000-0001-7655-5000

References

Adhikari, L., Zank, G. P., Telloni, D., et al. 2017, ApJ, 851, 117
Adhikari, L., Zank, G. P., & Zhao, L. 2021, Fluids, 6, 368
Adhikari, L., Zank, G. P., Zhao, L. L., et al. 2020, ApJS, 246, 38
Argall, M. R., Hollick, S. J., Pine, Z. B., et al. 2017, ApJ, 849, 61
Bandyopadhyay, R., & McComas, D. J. 2021, ApJ, 923, 193
Bavassano, B., Dobrowolny, M., Mariani, F., & Ness, N. F. 1982, JGR, 87, 3617
Behannon, K. W., Acuna, M. H., Burlaga, L. F., et al. 1977, SSRv, 21, 235
Bieber, J. W., Wanner, W., & Matthaeus, W. H. 1996, JGR, 101, 2511
Bruno, R., & Carbone, V. 2013, LRSP, 10, 2
Burlaga, L. F. 1968, SoPh, 4, 67
Burlaga, L. F., & Klein, L. W. 1986, JGR, 91, 347
Burlaga, L. F., Scudder, J. D., Klein, L. W., & Isenberg, P. A. 1990, JGR, 95, 2229
Chandran, B. D. G., Dennis, T. J., Quataert, E., & Bale, S. D. 2011, ApJ, 743, 197
Chen, C. H. K. 2016, JPlPh, 82, 535820602
Chen, C. H. K., Bale, S. D., Bonnell, J. W., et al. 2020, ApJS, 246, 53
Chen, C. H. K., Bale, S. D., Salem, C., & Mozer, F. S. 2011a, ApJL, 737, L41
Chen, C. H. K., Bale, S. D., Salem, C. S., & Maruca, B. A. 2013, ApJ, 770, 125
Chen, C. H. K., Horbury, T. S., Schekochihin, A. A., et al. 2010a, PhRvL, 104, 255002
Chen, C. H. K., Mallet, A., Yousef, T. A., Schekochihin, A. A., & Horbury, T. S. 2011b, MNRAS, 415, 3219
Chen, C. H. K., Wicks, R. T., Horbury, T. S., & Schekochihin, A. A. 2010b, ApJL, 711, L79
Cho, J., & Vishniac, E. T. 2000, ApJ, 539, 273
Coleman, P. J. J. 1968, ApJ, 153, 371
Cranmer, S. R. 2010, ApJ, 710, 676
Dasso, S., Milano, L. J., Matthaeus, W. H., & Smith, C. W. 2005, ApJL, 635, L181
Duan, D., He, J., Bowen, T. A., et al. 2021, ApJL, 915, L8
Gallana, L., Fraternale, F., Iovieno, M., et al. 2016, JGRA, 121, 3905
Gazis, P. R., McDonald, F. B., Burger, R. A., et al. 1999, SSRv, 89, 269
Goldreich, P., & Sridhar, S. 1995, ApJ, 438, 763
Goldreich, P., & Sridhar, S. 1997, ApJ, 485, 680
Hamilton, K., Smith, C. W., Vasquez, B. J., & Leamon, R. J. 2008, JGRA, 113, A01106
He, J., Tu, C., Marsch, E., & Yao, S. 2012, ApJL, 745, L8
He, J., Tu, C., Marsch, E., Bourouaine, S., & Pei, Z. 2013, ApJ, 773, 72
He, J., Wang, Y., Zhu, X., et al. 2022, ApJ, 933, 220
Heinemann, M., & Olbert, S. 1980, JGR, 85, 1311
Hollick, S. J., Smith, C. W., Pine, Z. B., et al. 2018, ApJ, 863, 76
Hollweg, J. V. 1974, JGR, 79, 1539
Horbury, T. S., Forman, M., & Oughton, S. 2008, PhRvL, 101, 175005
Howes, G. G., Bale, S. D., Klein, K. G., et al. 2012, ApJL, 753, L19
Iovieno, M., Gallana, L., Fraternale, F., et al. 2016, EJMF, 55, 394

Isenberg, P. A., Smith, C. W., Matthaeus, W. H., & Richardson, J. D. 2010, ApJ, 719, 716
Isenberg, P. A., Smith, C. W., & Matthaeus, W. H. 2003, ApJ, 592, 564
Joyce, C. J., Smith, C. W., Isenberg, P. A., Murphy, N., & Schwadron, N. A. 2010, ApJ, 724, 1256
Kiyani, K. H., Osman, K. T., & Chapman, S. C. 2015, RSPTA, 373, 20140155
Lee, M. A., & Ip, W. H. 1987, JGR, 92, 11041
Luo, Q. Y., & Wu, D. J. 2010, ApJL, 714, L138
Matthaeus, W. H., Goldstein, M. L., & Roberts, D. A. 1990, JGR, 95, 20673
Montgomery, D., Brown, M. R., & Matthaeus, W. H. 1987, JGR, 92, 282
Montgomery, D., & Turner, L. 1981, PhFl, 24, 825
Oughton, S., & Matthaeus, W. H. 2005, NPGeo, 12, 299
Oughton, S., Matthaeus, W. H., Wan, M., & Osman, K. T. 2015, RSPTA, 373, 20140152
Parashar, T. N., Goldstein, M. L., Maruca, B. A., et al. 2020, ApJS, 246, 58
Pearson, R. K., Neuvo, Y., Astola, J., & Gabbouj, M. 2016, EJASP, 2016, 87
Perez, J. C., & Chandran, B. D. G. 2013, ApJ, 776, 124
Pine, Z. B., Smith, C. W., Hollick, S. J., et al. 2020a, ApJ, 900, 91
Pine, Z. B., Smith, C. W., Hollick, S. J., et al. 2020b, ApJ, 900, 93
Pine, Z. B., Smith, C. W., Hollick, S. J., et al. 2020c, ApJS, 250, 14
Pine, Z. B., Smith, C. W., Hollick, S. J., et al. 2020d, ApJ, 900, 92
Podesta, J. J. 2009, ApJ, 698, 986
Roberts, D. A. 1990, JGR, 95, 1087
Roberts, D. A., Goldstein, M. L., Klein, L. W., & Matthaeus, W. H. 1987, JGR, 92, 12023
Santolík, O., Parrot, M., & Lefeuvre, F. 2003, RaSc, 38, 1010
Schekochihin, A. A., Cowley, S. C., Dorland, W., et al. 2009, ApJS, 182, 310
Shebalin, J. V., Matthaeus, W. H., & Montgomery, D. 1983, JPlPh, 29, 525
Smith, C. W., Aggarwal, P., Argall, M. R., et al. 2017, JPhCS, 900, 012018
Sokół, J. M., Kubiak, M. A., & Bzowski, M. 2019, ApJ, 879, 24
Sokół, J. M., Kucharek, H., Baliukin, I. I., et al. 2022, SSRv, 218, 18
Telloni, D., Carbone, F., Bruno, R., et al. 2019, ApJ, 887, 160
Torrence, C., & Compo, G. P. 1998, BAMS, 79, 61

Tu, C. Y., & Marsch, E. 1994, JGR, 99, 21
Tu, C. Y., & Marsch, E. 1995, SSRv, 73, 1
Tu, C. Y., Pu, Z. Y., & Wei, F. S. 1984, JGR, 89, 9695
Usmanov, A. V., Goldstein, M. L., & Matthaeus, W. H. 2016, ApJ, 820, 17
van der Holst, B., Sokolov, I. V., Meng, X., et al. 2014, ApJ, 782, 81
Vellante, M., & Lazarus, A. J. 1987, JGR, 92, 9893
Velli, M. 1993, A&A, 270, 304
Verscharen, D., Klein, K. G., & Maruca, B. A. 2019, LRSP, 16, 5
Wang, T., He, J., Alexandrova, O., Dunlop, M., & Perrone, D. 2020, ApJ, 898, 91
Whang, Y. C. 1973, JGR, 78, 7221
Wicks, R. T., Roberts, D. A., Mallet, A., et al. 2013, ApJ, 778, 177
Williams, L. L., & Zank, G. P. 1994, JGR, 99, 19229
Wu, H., Tu, C., Wang, X., et al. 2021, ApJ, 912, 84
Yan, L., He, J., Zhang, L., et al. 2016, ApJL, 816, L24
Zank, G. P. 1999, SSRv, 89, 413
Zank, G. P. 2016, GSL, 3, 22
Zank, G. P., Adhikari, L., Hunana, P., et al. 2017, ApJ, 835, 147
Zank, G. P., Adhikari, L., Zhao, L. L., et al. 2018, ApJ, 869, 23
Zank, G. P., & Matthaeus, W. H. 1992, JGR, 97, 17189
Zank, G. P., & Matthaeus, W. H. 1993, PhFlA, 5, 257
Zank, G. P., Matthaeus, W. H., & Smith, C. W. 1996, JGR, 101, 17093
Zank, G. P., Nakanotani, M., Zhao, L. L., Adhikari, L., & Telloni, D. 2020, ApJ, 900, 115
Zank, G. P., Zhao, L. L., Adhikari, L., et al. 2023, ApJS, 268, 18
Zhao, L. L., Zank, G. P., Adhikari, L., et al. 2020, ApJ, 898, 113
Zhao, L. L., Zank, G. P., Adhikari, L., et al. 2022, ApJL, 934, L36
Zhao, L. L., Zank, G. P., He, J. S., et al. 2021, ApJ, 922, 188
Zhou, Y., & Matthaeus, W. H. 1989, GeoRL, 16, 755
Zhu, X., He, J., Duan, D., et al. 2023, ApJ, 953, 161
Zhu, X., He, J., Verscharen, D., & Zhao, J. 2019, ApJ, 878, 48
Zhu, X., He, J., Verscharen, D., Duan, D., & Bale, S. D. 2020, ApJL, 901, L3
Zirnstein, E. J., Möbius, E., Zhang, M., et al. 2022, SSRv, 218, 28